

A planetary environment and analysis chamber (PEACH) for coordinated Raman–LIBS–IR measurements under planetary surface environmental conditions

Pablo Sobron* and Alian Wang

A planetary environment and analysis chamber (PEACH) has been developed at Washington University in St. Louis, in order to perform *in situ* multiple spectroscopic measurements on geological samples under relevant planetary environmental conditions and to support future planetary missions, with particular interest on Mars. The pressure in the chamber can range from ambient to 3×10^{-2} mbar. The simulated atmospheric composition and pressure are regulated via a combination of needle and ball valves connecting the chamber with containers filled with premixed gas. The temperature of the samples can be controlled in a range from ambient to -100°C . The *in situ* analytical techniques implemented (and to be implemented) are laser Raman spectroscopy, laser-induced breakdown spectroscopy (LIBS), near-IR reflectance spectroscopy, mid-IR attenuated total reflectance spectroscopy, and microscopic imaging. The coordinated spectroscopic sensing on the same geological sample under well-controlled atmospheric conditions in the PEACH establishes a way to link the results from the laboratory experiments to the spectral data obtained by landed and orbital planetary exploration missions, which will facilitate understanding the surface processes by which mineral phases occur and their association with atmospheric changes. Copyright © 2011 John Wiley & Sons, Ltd.

Keywords: Mars; environmental chamber; Raman; LIBS; imaging

Introduction

The uncontested evidence that liquid water was once present on Mars' surface has awakened a remarkable astrobiological interest in that planet. Mars is relatively close to Earth, shows certain similarities with our own planet, has great significance in the solar system evolution history, and is technologically accessible to us. For all these reasons, Mars is the highest priority target for the search of extraterrestrial life. However, the study of other planetary surfaces such as Europa or Titan is also regarded as a priority nowadays to assess the astrobiological potential elsewhere in our solar system.^[1,2] The present conditions at the surface of other planetary bodies, namely atmospheric pressure and composition, temperature, and levels of radiation are almost certainly not conducive to the presence of life. However, signatures of extinct life might have been preserved in the surface and subsurface materials in the form of microfossils and isotopic or organic biosignatures.^[3,4] The study of biominerals can also yield some clues about the potential for extraterrestrial life.^[5,6] In the particular case of Mars, the scientific objectives of past and current landed missions have focused mainly on understanding atmospheric and surface/subsurface mineralogical and geological properties in order to answer questions about the past and the evolution of Mars throughout history. As such, the science payloads onboard missions to Mars such as the Viking 1 and 2 landers, the Pathfinder rover, the Mars exploration rovers (MER), and the Phoenix lander have not been able to conclude whether life was or was not present on Mars. The next-generation instruments slated for the upcoming missions to Mars (Mars Science Laboratory (MSL) and ExoMars) have been designed to provide further answers on the

habitability of the planet, to search for biosignatures, and to investigate the geological, biological, and atmospheric processes through the characterization of surface and subsurface materials.

There are inherent limitations for *in situ* astrobiological/mineralogical planetary exploration. Among others, the instrument capabilities are constrained by volume, mass, and power consumption that are imposed by mission design factors. In addition, since the scientific payloads are exposed to harsh environmental conditions, the detection limits of species by the instruments and the quality of the returned data are seriously affected in comparison to their terrestrial laboratory counterparts. One of the potential scenarios that a mission science team might face is receiving data from one or several instruments regarding, for instance, the chemical composition of a targeted mineral grain, and, upon processing these data, finding that they do not correlate with any of the mineral databases recorded by the instruments during the test phases in terrestrial laboratories. This situation does not necessarily imply that a new mineral phase has been discovered on another planet. A likely explanation might be that the information recorded from the mineral when interrogated under the particular environmental conditions of that planetary surface is different from that recorded under Earth

* Correspondence to: Pablo Sobron, Department of Earth and Planetary Sciences and McDonnell Center for Space Sciences, Washington University, St. Louis, MO 63130, USA. E-mail: psobron@levee.wustl.edu

Department of Earth and Planetary Sciences and McDonnell Center for Space Sciences, Washington University, St. Louis, MO 63130, USA

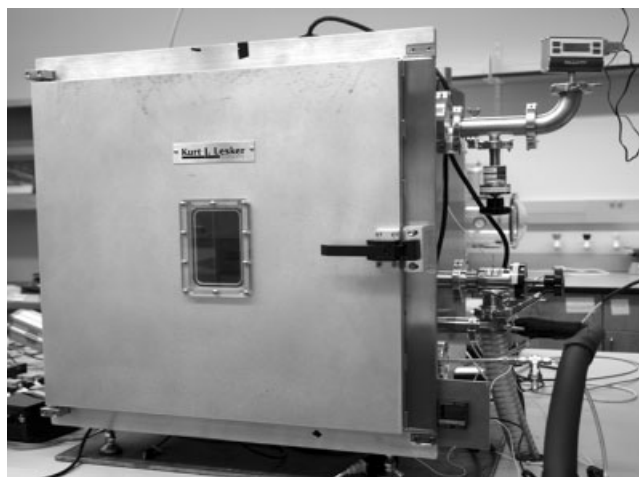


Figure 1. Photograph of the PEACH.

conditions. This phenomenon may be caused by unexpected material–atmosphere interactions and by unforeseen behavior of a flight instrument under specific environmental conditions during its deployment. Laboratory simulations provide the best means to evaluate the responses of planetary materials interrogated by flight instruments under given environmental conditions. Scientific studies of selected planetary (or planetary-relevant) materials carried out under simulated specific environmental conditions similar to those at the surface and the subsurface of a planet can help understand the processes by which mineral phases occur and are preserved, and their association with atmospheric changes. In addition, when such scientific studies are performed using techniques and instruments designed for planetary exploration, they can provide valuable support to the mission science teams on the detection limits of interesting species by the flight instruments, as well as other factors that need to be considered when interpreting the obtained mission data.

Considering the above possibilities, we have developed a planetary environment and analysis chamber (PEACH) containing multiple spectroscopic sensors that enable coordinated measurements to be made on the same set of geological samples under planetary-relevant environmental conditions, and to support future planetary missions, with particular interest on Mars. The PEACH (Fig. 1) is a stainless steel box-shaped sealed chamber manufactured by Kurt J. Lesker Company, with customized modifications including 2 viewports and 14 utility portholes. It is designed to allocate one imager and four spectroscopic probes inside. They are a laser Raman, a laser-induced breakdown spectroscopy (LIBS), a mid-IR (MIR), and a near-IR (NIR) probes and a microscopic imager (MI). The coordinated spectroscopic sensing on the same set of geological samples under well-controlled atmospheric conditions inside the PEACH establishes a way to link the results from the laboratory experiments to the spectral data obtained by, for instance, IR instruments onboard past and current landed and orbital Mars missions, such as OMEGA on Mars Express (MEX), MiniTES on MER, CRISM on Mars reconnaissance orbiter (MRO), and especially for the future MSL and ExoMars missions that include a LIBS spectrometer (ChemCam) and a Raman laser spectrometer (RLS) in their science payloads, respectively.

There are a number of planetary chambers designed to perform spectroscopic measurements of materials under simulated environmental conditions corresponding to different planetary

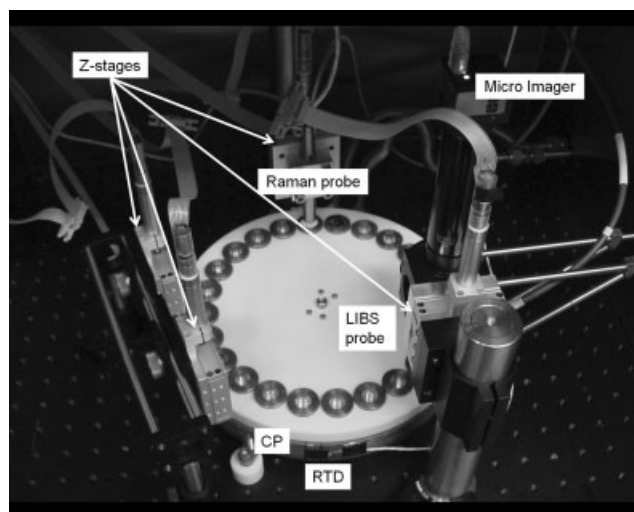


Figure 2. Photograph of the interior of the PEACH. The CP, the RTD sensor, the probe positioning stages (Z-stage), the Raman and LIBS probes, and the microimaging camera are labeled.

surfaces. Among them (a) the Mars environment (ME) and mini-ME^[7] have been designed to perform NIR reflectance spectroscopy of various minerals under Martian conditions, including a high dose of UV radiation, through a series of viewports; (b) the Andromeda^[8] is used to collect reflectance and emission spectra of analogs of Martian surface materials under atmospheric and temperature conditions similar to those at the Martian surface; and (c) the planetary environmental simulation chamber^[9] can perform UV and IR spectroscopy on samples exposed to a wide range of pressures, temperatures, and gas compositions. The (a) and (b) chambers are designed to operate in high vacuum (10^{-4} to 10^{-9} mbar), whereas the (c) chamber generates ultrahigh vacuum (10^{-10} mbar). However, because all the spectroscopic measurements performed in these chambers are made remotely through viewports mounted on the chamber walls (with spectrometers or probes residing outside the chambers), the data quality and accuracy is affected by the changes of sample surface relative to instrument focal plane, and by the atmospheric zones and boundaries.

Unlike the aforementioned chambers, the design of the PEACH allows conducting a set of Raman/LIBS/MIR/NIR/MI close-up measurements (coordinated or independent) on the same set of samples under the same environmental conditions. This is possible thanks to optical fiber technology (vis and IR) and to a sample positioning system that enables a sequential delivery of the individual samples to the focal plane of all the probes installed inside the PEACH. Using the instrumentation inside the PEACH, *in situ*, noninvasive, and coordinated spectral analysis of a sample under given environmental conditions can be achieved within minutes. Figure 2 shows a picture of the interior of the PEACH, including the currently installed Raman, LIBS, and MI probes. The choice of the spectroscopic techniques (Raman, LIBS, MIR, and NIR) makes the PEACH an ideal tool for Mars investigations. All the materials observed to date and expected to be found at Mars surface can be analyzed inside the PEACH under simulated Mars atmospheric conditions with these techniques, which have been (or will be) flown to Mars. The PEACH has the potential to provide a multispectral library of Mars-relevant materials that can be used in present (MER, MEX, MRO) mission data analysis and for future missions (MSL, ExoMars) for unambiguous identification

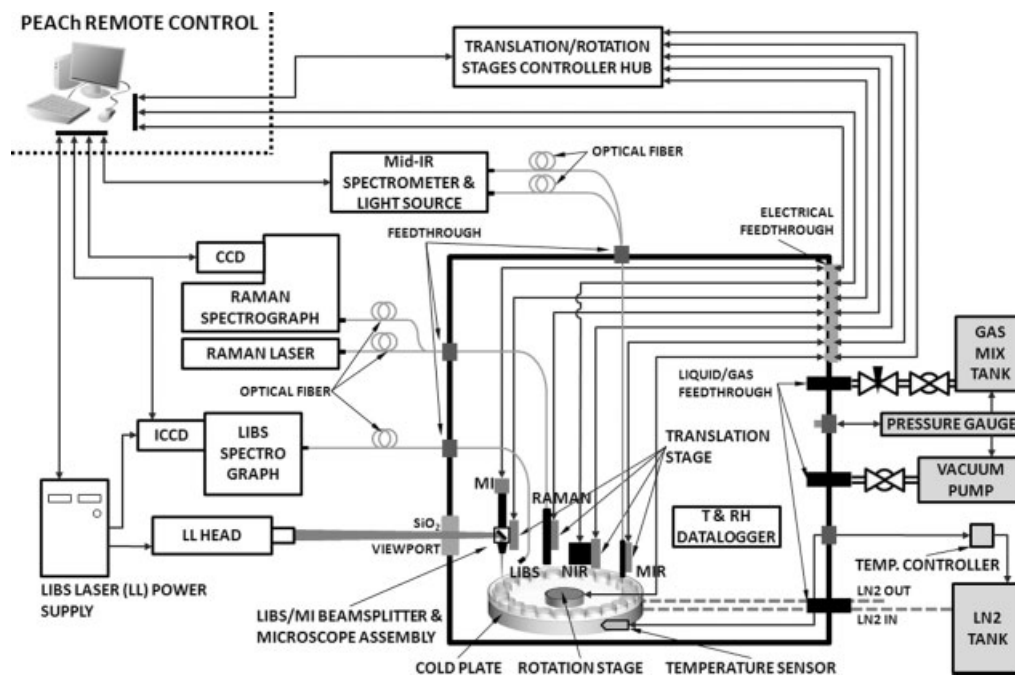


Figure 3. Functional diagram of the PEACH, showing all the elements installed (and to be installed) in the interior and exterior.

of mineral phases and chemical species. There is also potential for simulating the atmospheric conditions at the surfaces of other planetary bodies (e.g. Triton and Pluto). The PEACH is, to the best of our knowledge, the first environmental simulation chamber that features five internal sensors for the study of different planetary materials under controlled environmental conditions.

Technical Description

The PEACH consists of a single-walled stainless box-shaped sealed chamber (24" × 24" × 24") featuring a hinged door, 2 viewports, and 14 utility portholes. The hinged door provides easy access to the interior of the chamber for setting up the samples to be interrogated, while its Viton O-ring ensures that the chamber is able to reach high vacuum levels. The utility portholes accommodate feedthroughs (as used here, a feedthrough is a device that transfers services, utilities, and signals through the PEACH walls) for four purposes: (1) allowing input and output of gas mixes to control the atmospheric pressure and composition; (2) allowing input and output of cooling fluid to control samples' temperature; (3) accommodating optical fiber cables for the spectroscopic sensors (Raman, LIBS, MIR); and (4) accommodating power and data wires to control the motorized positioning stages for sample delivery and the probes' focal adjustment, and to interact with the NIR and MI probes for sample analysis. A functional diagram of the PEACH is shown in Fig. 3. The next subsections provide a concise description of the components of the PEACH, which have been grouped into three major categories: environmental control, spectroscopic sensors, and sample delivery system.

Environmental control

We have identified four parameters that are essential to evaluate the spectral behavior of materials on planetary surfaces: atmospheric pressure, atmosphere composition, sample temperature,

and UV radiation. At the time this manuscript was written, all parameters except the last one could be actively controlled inside the PEACH. Atmospheric temperature and relative humidity (RH) inside the PEACH can be monitored but not controlled.

1. Atmospheric pressure/vacuum: A high-vacuum scroll pump (Edwards XDS35i) allows maintaining pressure inside the PEACH at levels ranging from 1×10^{-2} mbar to terrestrial laboratory atmospheric pressure. Relatively high-pressure atmospheres such as that of Mars (~ 7 mbar average) are easily achievable and precisely controllable by the use of this pump in combination with several valves. Although our setup does not allow achieving the high or ultrahigh vacuum conditions at the surfaces of, for instance, the Moon and Jupiter's satellite Europa, the atmospheric pressures of other planetary bodies such as Neptune's moon Triton and Pluto can be easily simulated. Pressure is monitored with a convection-enhanced Pirani gauge (Kurt J. Lesker Company model KJL300808). Two bellows-sealed angle valves are used as vacuum and venting valves.
2. Atmosphere composition: The scroll pump described above runs continuously, thus allowing the maintenance of a constant atmospheric pressure by balancing inflow and outflow through a combination of ball and needle valves. The valves are used to allow the desired amounts of gas (or gas mixtures) from a single commercial tank enter the PEACH. At present, we use commercial calibrated gas mixtures that simulate realistic planetary atmosphere compositions.
3. Sample temperature: The average recorded temperature on Mars is -63°C with a maximum of 20°C (equatorial summer) and a minimum of -140°C (polar winter).^[10] With these numbers in mind, we have designed a purpose-built liquid nitrogen (LN2) storage and delivery interface that provides active control of the temperature of the samples inside the PEACH in the range 21 to -100°C . The LN2, stored in a Dewar outside the PEACH, is heated by a resistor immersed

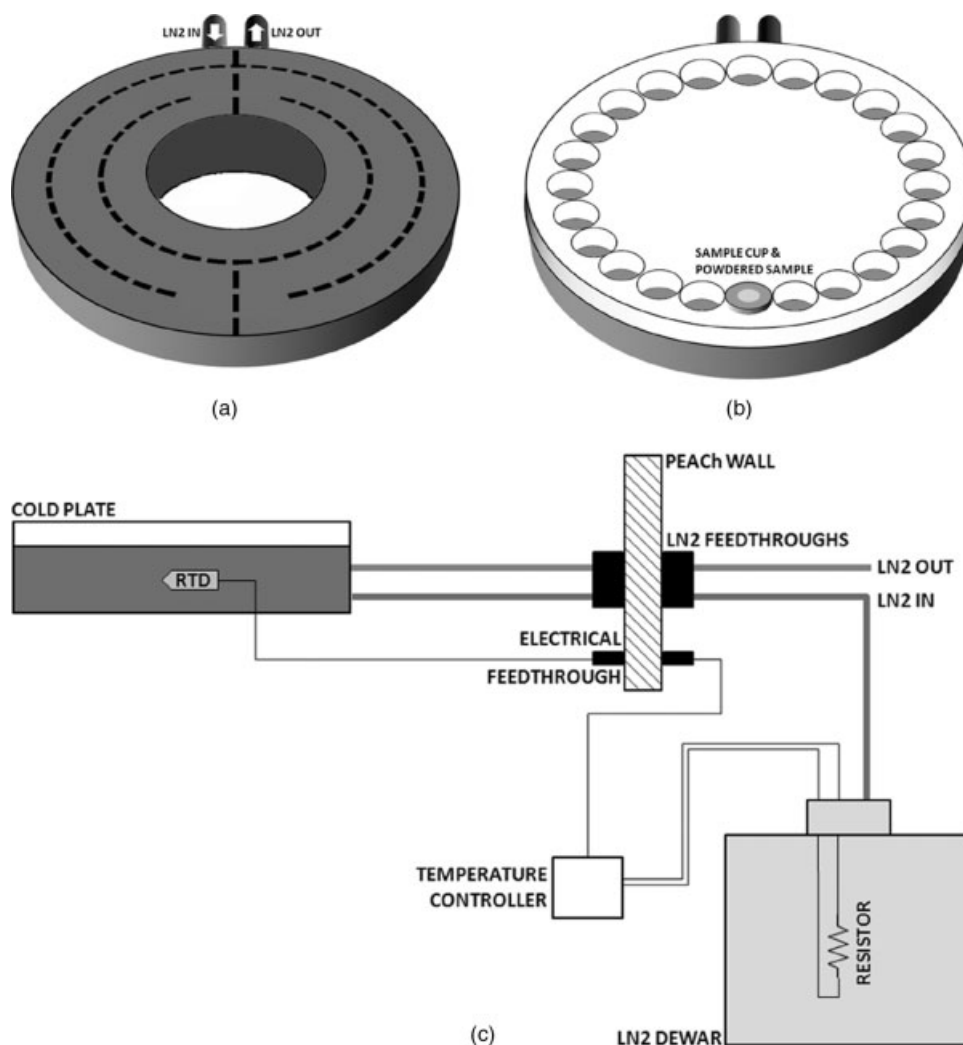


Figure 4. (a) Cartoon of the CP's interior wall design and inlet/outlet ports. (b) Cartoon of the Teflon disk and sample cup distribution. (c) Schematics of the cooling setup in both interior and exterior sides of the PEACH.

in the LN₂ reservoir and the evaporated N₂ gas at near-LN₂ temperature is directed via a feedthrough in the PEACH's wall into a toroid-shaped double-walled copper block (referred to as the cold plate (CP) hereafter) that sits inside the PEACH. Another feedthrough allows for the evacuation of the nitrogen gas (NG) after its circulation through the CP. An electronic controller (OMEGA Engineering Inc. CN76000 autotune controller) monitors the temperature of the CP via a resistive thermal device (RTD) element and regulates the flow of cold NG that enters the CP. This setup allows the temperature of the CP to be kept constant at a desired value (between 21 and -100°C) with deviations of less than 0.5°C . Figure 4 displays a diagram of the sample cooling setup. The CP alone is shown in Fig. 4(a). A total of 24 copper sample cups (containing powdered samples) are placed in contact with the CP. The high thermal conductivity of metal copper (sample cups and the CP) guarantees that, when the cold NG circulates through the CP, the entire system (CP cups and samples) is cooled down in a fairly homogeneous way, as shown in the performance tests reported in the section Temperature Distribution. A Teflon wheel, depicted in Fig. 4(b), holds and carries the 24 sample cups, ensuring that they are distributed

evenly along the outer edge of the CP. The design of the Teflon wheel guarantees good thermal contact between the sample cups and the CP and ensures accurate sample delivery to the spectroscopic sensors.

- UV radiation: Unlike that of Earth, the Martian surface is not protected by a dense atmosphere that absorbs the high dose of UV radiation coming from the Sun. Despite being farther away from the Sun, the daily UV flux Mars's surface is 361 kJ/m^2 compared to the 39 kJ/m^2 received daily on our planet.^[11] There is evidence of mineral photoalteration due to exposure to high doses of UV radiation on Mars.^[12] The dehydration kinetics of certain hydrated sulfates seems to be affected by exposure to UV radiation.^[13] It would be of great interest to study the Raman, LIBS, and IR spectral signatures of the alteration products of selected Mars-relevant materials when exposed to high UV radiation. For this reason, we have obtained further funding from the NASA Mars Fundamental Research Program to purchase and to install the optical fiber cable that will deliver the UV radiation from a xenon and/or deuterium lamp to the samples inside the PEACH.
- Ambient temperature (T) and RH: A combined T and RH probe (Extch Instruments RHT20 Datalogger) allows monitoring

Table 1. Derived RH inside the PEACH for given temperature and pressure

Pressure (mbar)	Temperature (°C)					
	0 (%)	-20 (%)	-40 (%)	-60 (%)	-80 (%)	-100 (%)
1000	>100	>100	>100	>100	>100	>100
100	16.07	95.11	>100	>100	>100	>100
10	1.61	9.51	76.49	>100	>100	>100
5	0.80	4.76	38.24	>100	>100	>100
1	0.16	0.95	7.65	90.93	>100	>100
0.5	0.08	0.48	3.82	45.47	>100	>100
0.1	0.02	0.10	0.76	9.09	>100	>100
0.05	0.01	0.05	0.38	4.55	89.28	>100
0.01	0.00	0.01	0.08	0.91	17.86	>100

The calculations are based on the saturated water vapor pressure for different temperatures reported by Haar *et al.*,^[15] assuming 40% RH in laboratory at 21 °C and 1 bar.

those two variables inside the PEACH. The RH values that can be achieved are within the range of partial pressure of water vapor near the surface of Mars.^[14] By way of an example, Table 1 shows the RH values that can be reached at given vacuum levels and sample temperatures inside the PEACH. A note must be made that the RH measured at pressure below than 10 mbar are subject to large instrumental error.

Spectroscopic sensors

The PEACH is equipped with five sensors that provide spectral information and contextual microscopic imagery of the samples under investigation. Only the Raman and LIBS probes and the MI camera were installed at the time of writing this manuscript. The MIR attenuated total reflection (ATR) sensor and optical fiber cables have been delivered and are currently being customized for installation inside the PEACH. The NIR sensor will be installed inside the PEACH upon completion of independent performance tests.

1. Raman sensor: the Raman probe is a stand-alone In Photonics Raman Probe. The working distance (~5 mm) of this Raman probe and the excitation laser wavelength (532 nm) are equivalent to those to be used in the RLS under development for the ExoMars mission.^[15] This probe has been installed inside the PEACH and is connected with an external laser unit and a RamanRxn1 spectrograph (Kaiser Optical Systems, Inc.) through two optical fibers. Both the laser unit and spectrograph sit outside the PEACH. A diode-pumped solid-state laser (Crystalaser) delivers up to 12 mW of 532 nm excitation light at the sample surface inside the PEACH. The laser spot at the sample surface is ~20 μm in diameter. An Andor DU401A-BV-132 iDus CCD camera attached to the RamanRxn1 spectrograph records the Raman spectra from the samples.
2. LIBS: Unlike the Raman probe, which uses an optical fiber for laser energy delivery, we decided to take a free-space energy delivery approach for the LIBS setup, because optical fibers are known to fail under the highly energetic Q-switched laser pulses required in common LIBS applications. The damage threshold for a typical silica glass surface using the type of laser required for LIBS is ~5 GW/cm²,^[16] although fiber failure has been observed at power densities as low as 1.5 GW/cm².^[17] In our free-space laser beam delivery approach, a quartz fused silica viewport mounted on the wall of the PEACH allows a pulsed laser beam to enter the PEACH and to be focused onto the surface of a sample, thus creating a plasma plume. An energy-adjustable Nd:YAG laser (Minilite-II by Continuum, Inc.) is used to generate high-intensity laser pulses at a wavelength of 1064 nm that deliver up to 30 mJ per pulse at the sample surface. Pulses are 7 ns in duration and can be generated at a maximum of 15 Hz rate. The laser pulses entering the PEACH are deflected by a high IR-efficiency OFR metallic front-surface beamsplitter and focused onto the sample surface via an OFR 5× microscope objective optimized for 1064 nm high-power YAG laser applications. The laser spot size at the sample surface is ~100 μm in diameter. A bare UV-enhanced optical fiber (230 μm core diameter) positioned at ~10 mm and 45° from the surface of the sample collects the light from the plasma and transmits it to a Mechelle 5000 spectrograph (Andor) equipped with an intensified CCD (Andor iStar) located outside the PEACH. This spectrometer (200–950 nm) covers the full spectral range of the ChemCam instrument on MSL rover, with a higher spectral resolution (0.04–0.1 nm). A note should be made here that ChemCam is designed for analyses of remote targets (1–7 m) and is equipped with three spectrometers. It uses a multiplexer to split and deliver the incoming photons into three spectral ranges (225–320, 381–471, and 497–528 nm) for simultaneous analysis at resolutions ranging from 0.09 to 0.3 nm.^[18] Compared to MSL's ChemCam, our LIBS setup in the PEACH provides a wider spectral range, higher spectral resolution, and higher collection efficiency (0.0066 vs ChemCam's 0.0033 – based on current ChemCam specifications). The major difference between our LIBS setup and ChemCam is, however, that we operate in the close-up mode (working distance ~10 mm), and coordinate it with a close-up Raman mode. We are considering upgrading our setup by adding stand-off LIBS capability to measure the samples in PEACH, in order to evaluate the distance effect (i.e. the different response of LIBS emission lines to distance) and to collect the LIBS spectra by close-up and by remote measurements, thereby to gain a better understanding of the data that will be obtained by the MSL ChemCam during its deployment on Mars' surface.
3. MI: The MI camera is placed on top of the LIBS focusing optics, and shares the same OFR 5× microscopic objective. Reflected light coming from the sample passes through the beamsplitter described in (2) and is collected by an Edmund Optics GigE video camera. The camera features a highly sensitive CMOS detector that provides a resolution of 1.05 μm/pixel when used in conjunction with a 10× magnification in-line lens assembly unit (Edmund Optics Infnititube) and the OFR 5× microscopic objective. The field of view of the MI is 1.34 × 1.08 mm. An electrical feedthrough is used to control the camera acquisition parameters and to download the image data to a computer outside the PEACH.
4. Near-IR sensor: It is an active reflectance NIR spectrometer (Water IR, or WIR) that covers two spectral ranges (1.25–2.53 and 2.5–5.0 μm) with a total of 256 spectral channels, i.e. a very similar spectral range as MEX OMEGA C and L spectrometers with comparable spectral resolution and higher sensitivity. The WIR-III has a unit volume of 3' × 2' × 3' and mass of 294 g, and was developed under an ASTID project.^[19,20] It underwent

a successful field deployment at the saline playas on the Tibet Plateau.^[21] Recently, the key element of this spectrometer has passed a low-temperature test at -29°C and a radiation test at 7.0 kRad at a cyclotron facility. The WIR will be installed inside the PEACH upon conclusion of the current ASTID project.

- Mid-IR sensor: It is an ATR mid-IR probe. The ATR probe has a diamond tip and is attached to a polycrystalline infrared (PIR) optical fiber cable (PIR, using AgCl : AgBr solid solution crystals). The spectral coverage is $3300\text{--}550\text{ cm}^{-1}$ and can work in the 4–420 K temperature range. The MIR optical fiber cable will be connected to a Nexus 670 FTIR spectrometer placed outside the PEACH. Upon installation, the information from MIR-ATR measurements will be helpful for the data interpretation of the MiniTES instrument on MER.
- Motorized positioning systems: The four probes (LIBS and MI are considered as one hereafter as they share the beamsplitter/microscope objective module) are mounted on motorized stages that allow them to travel in an axis perpendicular to the surface of the samples, thus providing focusing capability. The Thorlabs MT Series Translation Stages used inside the PEACH have been upgraded for operation in vacuum. They feature DC servomotors that position the probes with sub-micrometer resolution and full displacement of 12 mm, and are controlled remotely from a computer outside the PEACH.

Sample temperature control and sample delivery to sensors

We have designed a sample positioning and delivery system that allows the samples to be sequentially presented to each of the five sensors, which sit in fixed locations around the CP, inside the PEACH. A Teflon wheel holds 24 sample cups in place along the outer edge of the CP and helps in maintaining the thermal contact between the sample cups and the CP, thus ensuring simultaneous cooling of the CP, cups, and samples. The Teflon wheel is disc-shaped and has the same external diameter as the CP. It is connected to a high-torque, high-resolution, and vacuum-grade motorized rotation stage that sits in the void at the center of the toroidal CP. When the rotation stage actuates, the Teflon wheel plus the 24 sample cups rotate while the CP remains in place. The motorized rotation stage (Thorlabs CR1-Z7) features a 5 arcmin resolution (which translates into less than $10\text{ }\mu\text{m}$ in a longitudinal scale). This guarantees that the same sampling spot in a sample cup under investigation is delivered to the field of view of each of the spectroscopic sensors.

Concept of operation

A typical low-temperature experiment under Mars atmospheric conditions with Raman, LIBS, MIR, and NIR sensing consists of eight stages: (1) powdering the samples and placing them in the sample cups; (2) generating proper vacuum inside the PEACH (for practical purposes, pressure is typically reduced to 7×10^{-2} mbar only because of the long time it would take to achieve the absolute minimum pressure in the PEACH: see Table 2 and explanation in section on Potential calibration targets for RLS: Si wafer and diamond); (3) pumping 7 mbar of a gaseous mix composed almost entirely of CO_2 into the PEACH; (4) cooling down the samples to a preselected temperature; (5) recording micrographs (MI probe) of the samples; (6) delivering the samples to the nondestructive probes (Raman, MIR, and NIR); (7) delivering the samples to the LIBS probe; and (8) recording micrographs (MI probe) of the samples after LIBS measurement.

Table 2. Measured pressure inside the PEACH as a function of time during the high vacuum generation stage in two configurations: (a) No feedthroughs (optical fiber cables and electric cables) installed, and (b) feedthroughs for spectroscopic and temperature sensors installed

(a)		(b)	
Time (min)	Pressure (mbar)	Time (min)	Pressure (mbar)
0	1060	0	1060
1	128	1	270
2	10	2	18
3	1	3	2
4	0.250	4	0.600
5	0.200	5	0.400
10	0.120	10	0.200
15	0.090	15	0.170
20	0.070	20	0.150
25	0.060	25	0.130
30	0.055	30	0.120
45	0.042	45	0.100
60	0.034	60	0.080
75	0.030	75	0.075
90	0.026	90	0.071
120	0.021	120	0.062
150	0.018	150	0.055
180	0.016	180	0.049
210	0.014	210	0.044
240	0.013	240	0.039
270	0.012	270	0.370
300	0.011	300	0.035
330	0.010	330	0.033
360	0.010	360	0.031
390	0.009	390	0.030

Performance Tests

A set of tests was carried out to evaluate the performance of the PEACH regarding vacuum and cooling capabilities.

Vacuum tests

Table 2 reports the measured pressure inside the PEACH as a function of time during the high-vacuum generation stage in two configurations: (a) no feedthroughs (optical fiber cables and electric cables) installed, and (b) feedthroughs for spectroscopic and temperature sensors installed. The PEACH uses three types of feedthroughs (Kurt J. Lesker Company): electrical, fluid, and epoxy-filled. The electrical feedthroughs used in the PEACH are ultrahigh vacuum-rated and transfer electrical power and signals (data) through the walls. The fluid feedthroughs are used to transfer the gas mixtures and cooling NG into the PEACH. Both air and vacuum sides of these feedthroughs are terminated with Swagelok fittings. Epoxy-filled feedthroughs are used for the optical fibers and the temperature sensor's wires. The Varian Torr Seal epoxy forms a seal between the optical fibers and wires and the vacuum wall through which they pass. Epoxy-filled feedthroughs present a number of disadvantages compared to optical feedthroughs (typically a silica core welded into a specific flange with the optical fiber elements coupled to either end), e.g. difficult dismantlement upon assembly and poor leak tightness. However, optical feedthroughs were not considered in the design of the PEACH because they suffer from considerable

Table 3. Temperature of the CP as a function of time

Time (min)	Temperature (°C)
0	21
15	-15
20	-30
28	-50
47	-75
51	-80
58	-85
65	-90
76	-95
92	-100
100	-101
106	-102
113	-102
120	-103

transmission losses and constrain the transmission of light to specific wavelength ranges.

Among the causes for vacuum leaks in the PEACH, the use of the feedthroughs described above accounts for the most part. A total of 14 feedthroughs are currently used or expected to be used in the chamber. However, there are other factors that contribute to vacuum leakage; the partial degassing of the samples and the instrumentation installed inside the PEACH and the poor sealing of the optical fiber ends and the probes are noteworthy. The difference in the values of the vacuum generated inside the PEACH (Table 2) when feedthroughs are or are not installed gives an idea of these vacuum leaks. For practical purposes, a pressure of 0.07 mbar is achieved after 90 min of vacuum pump operation in a real experiment scenario, i.e. with all of the feedthroughs installed. This represents a mere 1% of the average Martian atmosphere, thus guaranteeing that, upon pumping the proper gas mixture, the atmosphere composition inside the PEACH will be essentially that of Mars.

Temperature tests

Minimum CP temperature

A test was performed to evaluate the minimum temperature achievable in the CP inside the PEACH. To simulate realistic experimental conditions, the 24 sample cups were filled with powdered gypsum and placed on top of the CP. The atmosphere inside the PEACH was kept constant at 7 mbar of CO₂ throughout the test. The values of the temperature of the CP as a function of time are reported in Table 3. The minimum CP temperature achieved was -103 °C.

Temperature distribution

The CP was designed to provide, as far as possible, homogeneous cooling across the top surface of the copper toroid, where sample cups sit. Both CP and sample cups are made of copper, a metal that features high thermal conductivity. Manufacturing constraints imposed an inner design of the CP such as that shown in Fig. 4(a), where a series of walls define a pathway through which the NG at near-LN₂ temperature flows. The NG enters the CP through the input port, and removes heat from the copper block as it flows towards the exit port, thereby effectively cooling the CP

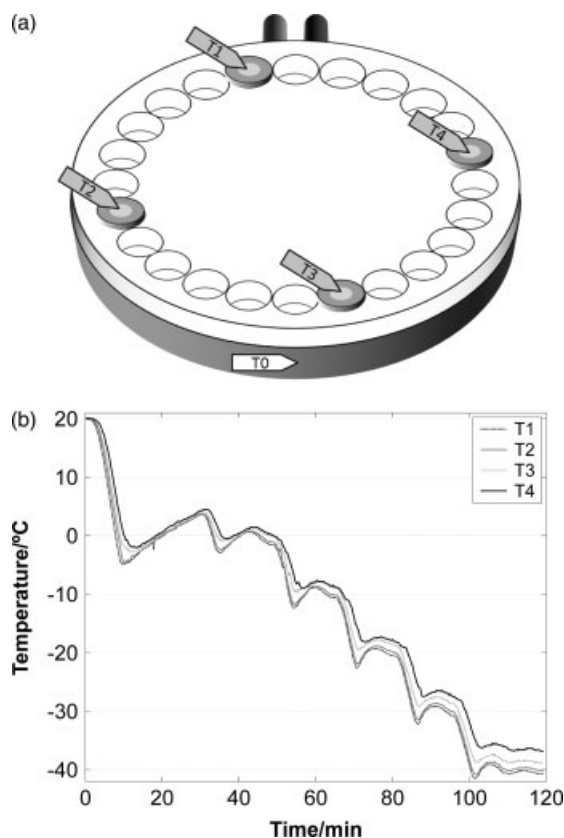


Figure 5. (a) Cartoon showing the positioning of the four samples used for the temperature measurements in the performance test. (b) Samples' measured temperature as a function of time for several programmed cooling profiles.

and the samples inside the sample cups. According to the energy conservation laws, the NG gets warmer in this process. As a consequence, and given the geometry of its inner walls (Fig. 4(a)), the left half of the CP is expected to be cooled faster than the right half. To evaluate this effect, we measured the temperature of four samples (jarosite powder) in four cups placed in the positions shown in Fig. 5(a) at different programmed CP temperatures. The temperature was measured at the surface of the samples by using thermocouples. Note that the control temperature (T_0), which is monitored by the temperature controller, is measured at the external face of the CP. Independent cooling tests showed that, when the system is programmed to cool the CP in temperature steps greater than 10 °C, the thermal inertia of the copper block makes the real temperature reach values up to 7° lower than the preset temperature. However, the real temperature stabilizes around the value of the programmed temperature soon after the temperature controller reconfigures the cooling profile. In general, a temperature stabilization time of 10 min is required to guarantee that the CP reaches the preset temperature.

For the current experiment, the atmospheric pressure inside the PEACH was kept constant throughout the test at 7 mbar of CO₂, and the starting sample temperature was 21 °C. The target temperature was first set to 0 °C. The overcooling effect described above can be observed in Fig. 5(b). More important is the fact that the temperature profiles of the samples in this first cooling event, and in fact throughout the entire cooling test, validate the assumption of nonhomogeneous cooling of the CP: the closer the sample to the NG inlet, the cooler it becomes. After the

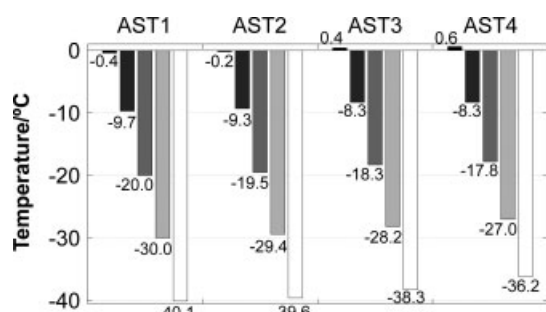


Figure 6. Values of the samples' AST measured for five different CP's programmed temperatures. Horizontal grids represent T_0 , the control temperature.

samples reached 0°C , the cooling system was turned off. As can be observed in the temperature profiles, the temperatures of the samples in the four measured cups tend to homogenize some 5 min after reaching the minimum temperature.

For the next stage in this test, the temperature controller was programmed to cool the samples in 10°C steps down to -40°C starting from 0°C . The controller also allowed 10 min for stabilization at each of the preset temperatures. The temperature profiles (Fig. 5(b)) follow a pattern similar to that observed in the $21-0^\circ\text{C}$ cooling step. There are, however, notable differences between the temperatures of the samples according to their position relative to the NG inlet. Figure 6 shows the values of the average stabilized temperatures (ASTs) of the samples at each of the five preset temperatures. AST# is defined as the average of the measured temperatures of a sample over the temperature stabilization period, typically 10 min, and # ranges 1–4 according to the position of the sample, as shown in Fig. 5(a). Only AST1 is consistent with the control temperature (T_0), showing slight or no deviation at all of the preset temperatures (Fig. 6). On the contrary, AST2, AST3, and AST4 are systematically higher than the preset temperatures, consistent with the hypothesis of a nonhomogeneous cooling of the samples due to design constraints. Another consequence of the chosen CP design is that, the lower the control temperature (T_0), the greater the temperature span between AST1 and AST4. In addition, when setting $T_0 < -20^\circ\text{C}$, temperature homogeneity cannot be reached, even after long period (Fig. 5). However, the unavoidable nonhomogeneous temperature distribution of the samples on the CP does not pose any limitation for the analysis of samples at known low temperature. Based on the values reported in Fig. 6, we have built a fitted linear regression model to correlate the temperatures of the samples with their absolute position on top of the CP and with the preset temperature. This solution allows predicting the temperature of a sample at any given position when the system is programmed to cool the CP within the 20 to -100°C temperature range with an accuracy of $\pm 1^\circ\text{C}$.

This test was done based on the fixed relative positions of sample cups to the CP. When performing coordinated (Raman–IR–LIBS) measurements of a set of samples, the Teflon wheel delivers the samples to different spectroscopic probes, thereby changing the position of the sample cups relative to the CP. This motion helps in homogenizing the temperatures of all the samples. An infrared thermocouple will be installed inside the PEACH to perform more accurate series of temperature measurements at the surface of 24 samples at given preset temperatures and positions. These measurements are expected to provide a means to optimize the sample cooling fitted model. In addition to this upgrade, the

effects of grain size distribution and thermal conductivity of the samples in the heat transfer mechanisms within the sample cups are also being studied.

Application I: Low-Temperature Raman Spectroscopic Study of Mars-Relevant Materials inside the Peach

Raman spectroscopy is based on the Raman effect, which is the inelastic scattering of photons by molecules. A small fraction of the scattered photons (10^{-6} to 10^{-9}) from a sample is wavelength-shifted by Raman effect with respect to the wavelength of the excitation wavelength.^[22] The wavelength shift depends on the molecular bonds and crystal structures in the sample interrogated by the excitation laser beam. In other words, Raman photons exhibit distinct energies (i.e. wavelengths) and scattering efficiencies (fingerprint spectral pattern) for particular molecular species and their structure. Therefore, information on the chemical composition and the structure of a given solid, liquid, or gaseous sample can be discerned from its characteristic Raman spectrum.

Among all other factors that affect Raman spectral features (e.g. temperature, pressure, resonance enhancement, and photoluminescence), temperature has a major influence on the Raman spectra obtained at a planetary surface, and can be straightforwardly investigated in the PEACH. An elegant explanation to the temperature effect in Raman spectral features is that the change of Raman peak positions, peak widths, and peak intensities results from anharmonic terms in the potential energy of molecular vibration,^[23] which is determined by the anharmonic potential constants, the phonon occupation number, and the thermal expansion of the crystal.^[24] Note that the Raman interaction involves either the absorption (Stokes Raman shift) or emission (anti-Stokes Raman shift) of a phonon, whose population in the lattice is dependent on temperature.^[25]

Raman spectroscopy will be used for the first time on another planetary surface during the ExoMars mission. An RLS placed inside the rover will analyze Martian subsurface powdered samples obtained by a deep drill. Although no data on the working temperature inside of ExoMars rover has been publicly disclosed by the European Space Agency to our knowledge, we can expect the temperature in the analytical laboratory inside the ExoMars rover to be somewhere between -40 and $+10^\circ\text{C}$ during the Raman measurements. As outlined above, the Raman spectral features of the analyzed samples will be influenced by the temperature at which the spectra will be acquired. Our objective is to quantify these changes as a function of temperature under Mars atmospheric conditions in PEACH and to evaluate and to correct the temperature effects towards the phase identification and characterization that will be made by a flight RLS during the ExoMars mission.

We used the Raman sensor installed inside the PEACH to monitor the changes in the Raman peak properties as a function of temperature. The measured laser power at the samples' surface was 9.5 mW. The acquisition time was set to 5 s, and a total of 30 spectra taken on the same spot were averaged. The Raman spectra collected were processed using a set of routines,^[26] which includes noise reduction algorithms based on fast Fourier transform, baseline calculations through linear interpolation, band Fourier self-deconvolution, and peak-fitting algorithms based on the Marquardt method.^[27] The positions of selected peaks for each of the investigated materials are reported in Table 4.

Table 4. Raman shift of relevant bands at different temperatures

Si									
21 °C (cm ⁻¹)	5 °C (cm ⁻¹)	-5 °C (cm ⁻¹)	-40 °C (cm ⁻¹)	-95 °C (cm ⁻¹)	Band assignment				
521.9	522.4	522.5	523.1	523.9	Si-Si				
Diamond									
1332.5	1332.7	1332.7	1332.9	1333.1	C-C				
H ₂ O									
21 °C (cm ⁻¹)	11 °C (cm ⁻¹)	-10 °C (cm ⁻¹)	-26 °C (cm ⁻¹)	-38 °C (cm ⁻¹)	-48 °C (cm ⁻¹)	-55 °C (cm ⁻¹)	-66 °C (cm ⁻¹)	-76 °C (cm ⁻¹)	Band assignment
3211.3	3208.7	3137.6	3130.6	3126.7	3123.5	3121.1	3118.4	3115.5	O-H stretching
MgSO ₄ · 7H ₂ O									
21 °C (cm ⁻¹)	5 °C (cm ⁻¹)	-5 °C (cm ⁻¹)	-40 °C (cm ⁻¹)	-95 °C (cm ⁻¹)	Band assignment				
365.5	365.1	367.2	367.2	368.4	Mg-O stretching				
463.6	464.1	461.7	463.9	465.1	ν ₂ (SO ₄)				
498.9	499.2	499.6	499.6	499.6	ν ₂ (SO ₄)				
513.5	513.5	512.4	514.8	514.3	ν ₂ (SO ₄)				
610.6	610.0	609.3	608.3	607.1	ν ₄ (SO ₄)				
635.0	635.6	636.1	637.0	638.2	ν ₄ (SO ₄)				
661.6	661.3	661.3	660.2	659.2	ν ₄ (SO ₄)				
978.3	978.3	978.3	978.3	978.3	ν ₁ (SO ₄)				
984.6	984.7	984.8	984.9	984.9	ν ₁ (SO ₄)				
1057.8	1058.1	1056.1	1057.0	1056.7	ν ₃ (SO ₄)				
1089.7	1089.4	1091.9	1091.2	1091.9	ν ₃ (SO ₄)				
1142.4	1143.2	1144.4	1144.8	1144.4	ν ₃ (SO ₄)				
3195.3	3099.3	3110.6	3122.1	3130.7	H ₂ O				
3275.2	3209.4	3201.0	3192.8	3194.0	H ₂ O				
3436.7	3255.9	3275.6	3254.5	3263.6	H ₂ O				
3530.2	3310.7	3339.2	3318.5	3319.0	H ₂ O				
	3428.1	3433.1	3390.1	3399.5	H ₂ O				
	3517.5	3520.3	3447.6	3452.5	H ₂ O				
			3546.7	3526.9	H ₂ O				
MgSO ₄ · 4H ₂ O									
423.9	417.8	416.9	423.8	421.5	ν ₂ (SO ₄)				
459.1	457.1	458.0	456.7	456.8	ν ₂ (SO ₄)				
479.9	480.1	480.1	480.2	481.2	ν ₂ (SO ₄)				
619.2	619.9	619.9	620.9	623.1	ν ₄ (SO ₄)				
666.8	666.5	666.6	668.3	670.3	ν ₄ (SO ₄)				
994.3	994.3	994.3	994.3	994.3	ν ₁ (SO ₄)				
1000.9	1000.9	1000.9	1001.0	1001.0	ν ₁ (SO ₄)				
1085.0	1084.7	1084.2	1083.2	1081.7	ν ₃ (SO ₄)				
1117.5	1118.0	1117.9	1117.9	1118.5	ν ₃ (SO ₄)				
1154.8	1154.5	1154.8	1154.5	1155.9	ν ₃ (SO ₄)				
1181.8	1182.8	1183.3	1184.3	1185.8	ν ₃ (SO ₄)				
3324.8	3322.1	3325.4	3323.4	3326.9	H ₂ O				
3396.1	3396.8	3396.1	3395.8	3394.0	H ₂ O				
3431.7	3432.1	3430.9	3430.6	3428.2	H ₂ O				
3483.0	3482.4	3481.8	3482.2	3484.4	H ₂ O				
3551.1	3552.3	3553.1	3554.0	3557.3	H ₂ O				

Table 4. (Continued)

<i>CaSO₄ · 2H₂O</i>					
316.8	318.3	318.4	320.3	323.3	H ₂ O
414.0	413.9	413.9	414.0	414.2	$\nu_2(\text{SO}_4)$
492.8	492.7	492.6	492.5	492.2	$\nu_2(\text{SO}_4)$
581.1	580.6	579.6	581.3	582.8	H ₂ O
618.2	618.5	618.7	619.2	620.3	$\nu_4(\text{SO}_4)$
670.2	670.3	670.2	670.5	670.9	$\nu_4(\text{SO}_4)$
999.3	999.3	999.3	999.3	999.3	$\nu_1(\text{SO}_4)$
1008.1	1008.2	1008.2	1008.4	1008.6	$\nu_1(\text{SO}_4)$
1116.8	1117.3	1117.0	1117.0	1115.3	$\nu_3(\text{SO}_4)$
1135.5	1136.0	1136.2	1136.8	1138.1	$\nu_3(\text{SO}_4)$
3403.4	3403.3	3403.4	3403.5	3404.5	H ₂ O
3491.1	3490.2	3489.6	3488.7	3485.7	H ₂ O
<i>CaSO₄.0.5H₂O</i>					
427.1	426.7	426.9	423.6	427.1	$\nu_2(\text{SO}_4)$
488.7	488.6	488.7	489.3	488.3	$\nu_2(\text{SO}_4)$
610.4	607.8	607.6	606.8	606.4	$\nu_4(\text{SO}_4)$
628.4	628.7	628.8	630.2	629.0	$\nu_4(\text{SO}_4)$
667.4	667.4	667.7	670.0	667.8	$\nu_4(\text{SO}_4)$
1005.2	1005.2	1005.2		1005.2	$\nu_1(\text{SO}_4)$
1014.8	1015.1	1015.1		1015.6	$\nu_1(\text{SO}_4)$
1112.3	1111.8	1111.4		1112.2	$\nu_3(\text{SO}_4)$
1128.1	1128.4	1128.2		1129.2	$\nu_3(\text{SO}_4)$
1148.4	1148.9	1149.0		1150.5	$\nu_3(\text{SO}_4)$
1164.9	1165.4	1165.8		1166.9	$\nu_3(\text{SO}_4)$
1179.2	1179.2	1178.8		1180.3	$\nu_3(\text{SO}_4)$
3553.0	3552.3	3553.0	3552.5	3553.7	H ₂ O
3613.9	3613.6	3613.8	3615.6	3612.8	H ₂ O
<i>CaSO₄</i>					
416.9	417.2	416.6	416.3	416.1	$\nu_2(\text{SO}_4)$
499.1	499.4	498.8	498.6	498.6	$\nu_2(\text{SO}_4)$
609.8	610.1	609.5	609.2	608.8	$\nu_4(\text{SO}_4)$
628.1	628.4	627.8	628.1	628.3	$\nu_4(\text{SO}_4)$
675.8	676.1	675.5	675.5	675.8	$\nu_4(\text{SO}_4)$
1006.2	1006.2	1006.2	1006.2	1006.2	$\nu_1(\text{SO}_4)$
1016.7	1017.0	1016.8	1017.1	1017.4	$\nu_1(\text{SO}_4)$
1112.5	1112.6	1112.6	1113.1	1112.8	$\nu_3(\text{SO}_4)$
1128.5	1129.0	1128.8	1129.1	1129.6	$\nu_3(\text{SO}_4)$
1159.1	1159.5	1159.4	1159.6	1160.1	$\nu_3(\text{SO}_4)$
<i>K₂SO₄</i>					
449.8	449.6	449.3	449.3	449.7	$\nu_2(\text{SO}_4)$
455.9	455.6	455.9	455.9	456.6	$\nu_2(\text{SO}_4)$
480.1	480.7	480.4	480.4	480.9	$\nu_2(\text{SO}_4)$
618.4	619.0	618.7	618.6	619.6	$\nu_4(\text{SO}_4)$
625.8	626.4	626.4	626.1	626.5	$\nu_4(\text{SO}_4)$
668.9	668.3	668.6	668.9	669.3	$\nu_4(\text{SO}_4)$
977.7	977.7	977.7	977.7	978.4	$\nu_1(\text{SO}_4)$
984.0	984.3	984.3	984.8	986.3	$\nu_1(\text{SO}_4)$
1093.2	1093.7	1093.2	1094.0	1094.5	$\nu_3(\text{SO}_4)$
1107.1	1107.4	1107.7	1107.2	1108.8	$\nu_3(\text{SO}_4)$
1138.8	1138.8	1139.0	1138.4	1139.8	$\nu_3(\text{SO}_4)$
1145.5	1145.7	1145.8	1146.3	1147.8	$\nu_3(\text{SO}_4)$

Table 4. (Continued)

<i>NaSO₄</i>					
369.8	370.7	371.0	371.3	371.1	Na–O stretching
411.0	410.1	409.8	409.5	408.9	$\nu_2(\text{SO}_4)$
451.5	450.6	450.3	450.0	449.4	$\nu_2(\text{SO}_4)$
466.9	467.8	467.8	467.9	468.1	$\nu_2(\text{SO}_4)$
621.2	621.1	620.9	621.0	621.2	$\nu_4(\text{SO}_4)$
633.9	633.7	633.8	633.9	633.6	$\nu_4(\text{SO}_4)$
647.8	648.1	648.1	648.4	649.0	$\nu_4(\text{SO}_4)$
986.7	986.7	986.7	986.7	986.7	$\nu_1(\text{SO}_4)$
993.3	993.5	993.5	993.7	994.0	$\nu_1(\text{SO}_4)$
1095.7	1096.1	1096.3	1096.7	1096.9	$\nu_3(\text{SO}_4)$
1101.7	1102.1	1102.2	1102.6	1103.0	$\nu_3(\text{SO}_4)$
1130.9	1131.6	1131.6	1131.9	1132.9	$\nu_3(\text{SO}_4)$
1151.9	1152.4	1152.4	1152.8	1153.6	$\nu_3(\text{SO}_4)$
<i>Pyroxene</i>					
21 °C (cm ⁻¹)	5 °C (cm ⁻¹)	-5 °C (cm ⁻¹)	-40 °C (cm ⁻¹)	-99 °C (cm ⁻¹)	Band assignment
387.1	387.0	385.5	386.1	386.6	M–O stretching
664.9	665.3	664.6	665.5	665.7	Si–O–Si
1011.2	1011.6	1011.9	1011.9	1012.4	Si–O stretching
<i>Olivine</i>					
822.6	823.1	823.0	823.3	823.4	Si–O stretching
854.0	854.1	854.0	853.9	854.1	Si–O stretching
<i>α-Quartz</i>					
464.1	464.3	464.4	464.7	465.5	Si–O–Si

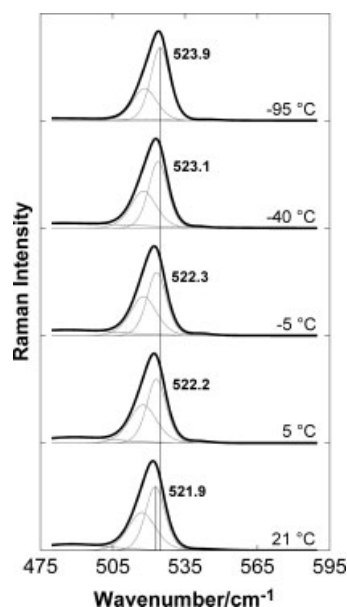


Figure 7. Raman spectra of Si wafer in the 475–590 cm⁻¹ spectral region at different temperatures. Labels indicate the position of the intense peak from spectral deconvolution.

Potential calibration targets for RLS: Si wafer and diamond

Silicon wafers are routinely used in Raman spectroscopy laboratories for wavelength calibration of the spectrometers because

they show a very strong and sharp peak near 521 cm⁻¹ at 20 °C. A silicon wafer or a silicon-coated target might also be used onboard ExoMars for the calibration of the RLS instrument. It is thus important to evaluate the Raman spectra of this material in the range of ExoMars working temperatures. Figure 9 shows the Raman peak from the Si–Si stretching mode of a silicon wafer collected at different temperatures using our Raman probe inside the PEACH. We have modeled the Raman peak of Si wafer at 520.7 cm⁻¹ (peak maximum at 21 °C) as the convolution product of an intense peak and a shoulder. The shoulder may be explained in terms of crystal quality (crystalline defects and thermal stress).^[28] The position of the intense peak, whose Raman shift is 521.9 cm⁻¹ at 21 °C, is used to monitor the temperature-induced Raman peak shift. The values of the peak position for Si wafer reported in Table 4 are those of the mentioned main peak after deconvolution. Figure 7 shows the spectra of the Si wafer at different temperatures. The spectra have been normalized and intensity-offset for comparison purposes. The Raman peak of Si shifts towards higher wavenumbers as temperature decreases following a linear relationship (SNOR = 0.0209; SNOR is the square of the norm of the residuals):

$$w_{\text{Si-Si}} = -0.017563T + 522.28 \quad (1)$$

where $w_{\text{Si-Si}}$ is the position (cm⁻¹) of the intense peak after the spectral deconvolution, and T is the temperature of the silicon wafer in °C. This trend is consistent with a Si–Si bond length decrease (lattice constant decrease) and the subsequent bond strengthening among Si atoms as temperature decreases, and is

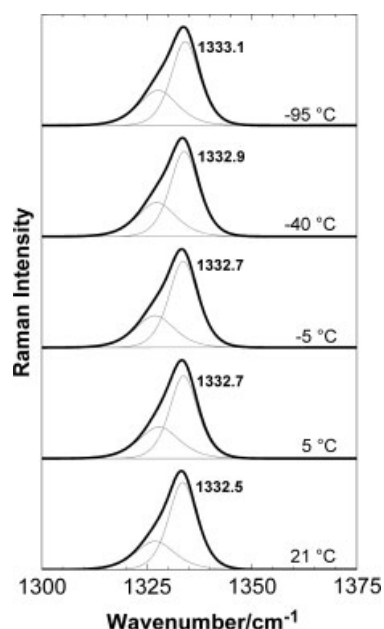


Figure 8. Raman spectra of natural diamond in the 1300–1375 cm^{-1} spectral region at different temperatures. Labels indicate the position of the intense peak from spectral deconvolution.

in agreement with previously reported temperature effects in the Raman scattering of silicon.^[29,30]

Natural diamond gives rise to a single sharp peak in the Raman spectrum at $\sim 1332 \text{ cm}^{-1}$ at 300 K.^[31,32] Fig. 8 shows the Raman spectra of natural diamond in the region 1300–1375 cm^{-1} for five different temperatures. Two peaks have been used to deconvolute the envelope of the Raman peak of diamond as shown in Fig. 8. Similar to Si wafer, the shoulder can be explained in terms of structural defects and particle size in the diamond chip used in this work.^[33] We use the position of the main peak to monitor the peak position shift as a function of temperature. This peak shifts slightly to higher wavenumbers as the temperature decreases. The following linear relationship has been derived (SNOR = 0.0099):

$$w_{C-C} = -0.009823 T + 1332.7 \quad (2)$$

where w_{C-C} is the position of the diamond intense peak in cm^{-1} , and T is the temperature of diamond in $^{\circ}\text{C}$. Solin and Ramdas^[32] (and references therein) have studied the effect of temperature in the position and width of this peak. Our results compare well with their observations. Borer *et al.*^[34] also calculated the position shift of the diamond Raman peak over a wider range of temperatures than used in this work. Their model assumes that the change in the vibration wavenumber is directly proportional to the relative change in volume of the diamond crystal subject to thermal expansion. We suggest that diamond could be a reliable temperature gauge for RLSs onboard landed missions.

Phases recently found on Mars: water and hydrated sulfates

The characterization of the interaction of the saline mineral assemblages identified at the Martian surface and the aqueous solutions necessary for their formation seems to be a priority for understanding Mars's hydrological and mineralogical history. Among others, hydrated minerals are particularly important. On the other hand, the investigation of the structural properties of ice

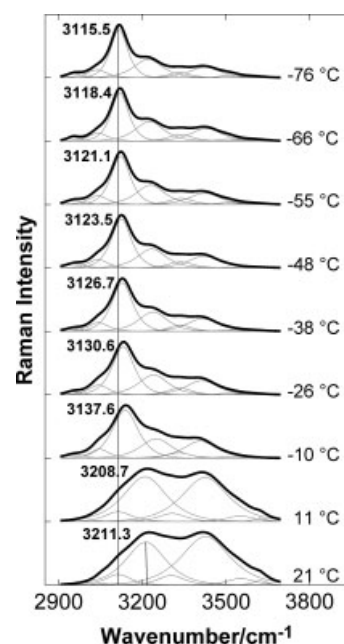


Figure 9. Raman spectra of water/ice in the 2900–3700 cm^{-1} spectral region at different temperatures. Labels indicate the position of the O–H ν_1 symmetric stretching vibrational peaks.

in planetary bodies (e.g. Mars ice caps, Europa, asteroids, etc.) may reveal clues about formation processes and constraints (mainly pressure and temperature) and atmosphere–surface material interactions. From the Raman spectroscopic point of view, the stretching vibrational modes of $\text{H}_2\text{O}/\text{OH}$ in the 3000–3800 cm^{-1} Raman spectral range are often used to characterize the hydration state of minerals^[35,36] and to investigate the structural properties of ices.^[37] The design of the PEACH allows *in situ* and noninvasive monitoring the evolution of the Raman peaks associated with O–H vibrations in any kind of sample as a function of temperature. Figure 9 shows the normalized and offset Raman spectra of water and water ice at different temperatures in the 2900–3700 cm^{-1} range. The spectrum of liquid water (21 and 11 $^{\circ}\text{C}$) is a complex envelope contributed by the symmetrical (ν_1) and asymmetrical (ν_3) stretching vibrations of O–H bonds in H_2O , the second overtone of symmetric bending of H–O–H bonds, and intra- and intermolecular couplings. When liquid water is cooled below the freezing point, the spectra change substantially, indicating transition from liquid water to ice. The spectral profile observed in the subzero spectra corresponds well with those observed in the spectra of ice Ih (a distribution of four molecules in a hexagonal cell) reported by Whalley.^[37] From 21 to $-76 \text{ }^{\circ}\text{C}$, we can readily observe a notable decrease of the ν_3 asymmetric Raman peak near 3410 cm^{-1} and a shift of the ν_1 symmetric Raman peak from 3211 to 3115 cm^{-1} as temperature decreases. These observations are consistent with the strong dependence of the O–H stretching vibration of water with the hydrogen-bond strengthening; lowering the temperature of the ice increases the strength of hydrogen bonding.

To evaluate the effect of temperature in the O–H stretching spectral region of hydrated minerals, we have recorded Raman spectra of synthetic epsomite ($\text{MgSO}_4 \cdot 7\text{H}_2\text{O}$), starkeyite ($\text{MgSO}_4 \cdot 4\text{H}_2\text{O}$), gypsum ($\text{CaSO}_4 \cdot 2\text{H}_2\text{O}$), and bassanite ($\text{CaSO}_4 \cdot 0.5\text{H}_2\text{O}$) in a temperature range from 21 to $-95 \text{ }^{\circ}\text{C}$. The normalized and offset spectra of the $\text{MgSO}_4 \cdot 7\text{H}_2\text{O}$ temperature series is plotted

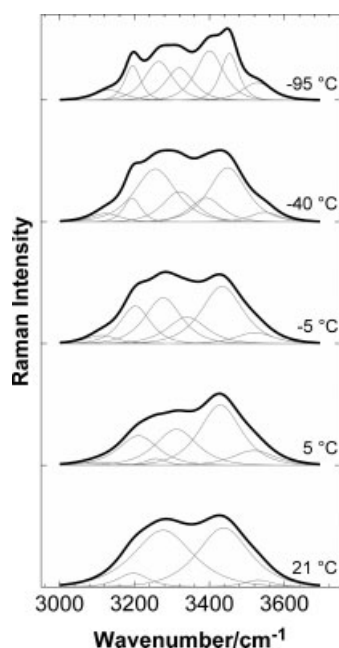


Figure 10. Raman spectra of epsomite in the 3000–3700 cm^{-1} spectral region at different temperatures.

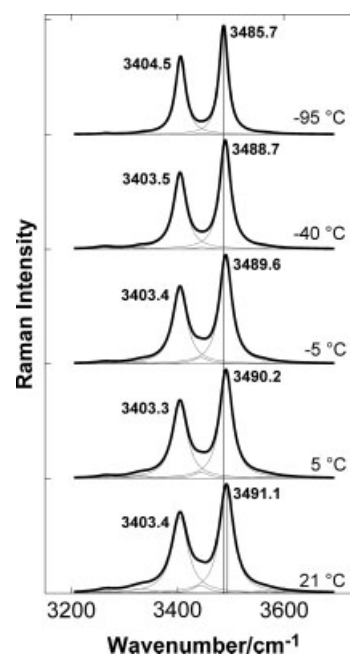


Figure 11. Raman spectra of gypsum in 3200–3700 cm^{-1} spectral region at different temperatures.

in Fig. 10 ($\text{H}_2\text{O}/\text{OH}$ modes only). The spectra of $\text{MgSO}_4 \cdot 7\text{H}_2\text{O}$ show overlapped water O–H stretching vibrations and overtone of water bending vibrations (e.g. the peak at around 3510 cm^{-1}). It can be seen that the peak widths decrease as the temperature is lowered. This allows a better deconvolution of the overlapped Raman peaks and a more accurate characterization of the peak features. This reduction in peak widths is mainly due to a decrease of the thermal broadening at low temperature. Another interesting effect associated with sample cooling is the rise of new peaks at low temperatures ($-95 \text{ }^\circ\text{C}$). This phenomenon seems to be due to an increase of structural ordering of the water molecules^[38] in epsomite crystal lattice and the formation of a low-temperature form of $\text{MgSO}_4 \cdot 7\text{H}_2\text{O}$ that has a specific stability field.^[39]

Figure 11 shows the normalized and offset spectra of the $\text{CaSO}_4 \cdot 2\text{H}_2\text{O}$ at different temperatures (H_2O modes only). The two distinct peaks arise as a consequence of the presence of two O–H bonds in the structural water molecules within the unit cell of gypsum featuring different bond lengths. The higher wavenumber peak near 3491 cm^{-1} is assigned to the O–H bond with a shorter bond length (0.944 \AA), $\nu(\text{O}_w\text{--H}(2))$, whereas the lower wavenumber peak near 3403 cm^{-1} is ascribed to the O–H bond with the longer bond length (0.962 \AA), $\nu(\text{O}_w\text{--H}(1))$.^[40,41] When temperature decreases, the peak position and width of the $\nu(\text{O}_w\text{--H}(2))$ mode decrease. The $\nu(\text{O}_w\text{--H}(1))$ peak shows less obvious increase in Raman shift and narrowing of the peak width. Our observation is consistent with a similar study^[41] performed over a much wider temperature variation range ($33\text{--}373 \text{ K}$). The behavior of both peaks has been explained in terms of the strengthening of hydrogen bonds as temperature decreases.^[41]

Silicate minerals on Mars: pyroxene, olivine, and quartz

Pyroxene-rich and olivine-rich basaltic rocks are widespread on Mars.^[42–44] Investigating the compositional features of the olivine and pyroxene grains in basaltic rocks can help understand ancient Martian volcanic processes and hydrothermal

episodes that have shaped Mars's surface and probably generated sulfate and phyllosilicate deposits around the globe. The Raman peak positions of pyroxenes and olivine depend strongly on their compositions.^[45,46] The Raman spectra of pyroxene are characterized by a complex envelope of peaks around 385 cm^{-1} (associated to M–O vibrations, M being a metal), a single peak or doublet in the $650\text{--}700 \text{ cm}^{-1}$ region (associated with Si–O_b–Si vibrations), and a strong peak or doublet around 1010 cm^{-1} (assigned to the Si–O_{nb} stretching mode).^[45–47] The Si–O_{nb} stretching vibration peak of the examined pyroxene sample shifts slightly towards higher wavenumbers as temperature decreases (Table 4). This is consistent with an increase in the strength of Si–O_{nb} bond induced by thermal contraction.^[48]

The Raman spectra of olivine has a characteristic pair of intense peaks at around 825 and 850 cm^{-1} , corresponding to the ν_3 asymmetric and ν_1 symmetric stretching vibrations of the Si–O bonds, respectively.^[49] A different assignment has been reported in which the olivine doublet is contributed by coupled ν_1 and ν_3 modes. The ν_1 mode contributes more to the $\sim 850 \text{ cm}^{-1}$ peak, whereas the ν_3 contributes more strongly to the $\sim 825 \text{ cm}^{-1}$ peak.^[50] Regardless, we do not observe a significant variation in the position of the $\sim 825 \text{ cm}^{-1}$ peak and only a slight upshift of the $\sim 850 \text{ cm}^{-1}$ peak as the temperature decreases (Table 4). Because the peak positions of the olivine doublet will likely be used to extract the information on Mg and Fe cation ratios during RLS measurements, this slight temperature-induced shift in the $\sim 850 \text{ cm}^{-1}$ peak of olivine will have to be taken into account.

SiO_2 -enriched rock nodules and regolith have been found on Mars by the Spirit rover in the Gusev crater.^[51] MiniTES spectral analysis suggested an amorphous opal structure, having not converted to crystalline quartz. The Raman spectrum of quartz features a strong band at around 464 cm^{-1} associated with Si–O vibration within the Si–O–Si structure.^[52] The Raman shift of this peak increases as temperature decreases, as a consequence of the aforementioned thermal contraction effect and decrease in the anharmonicity.

Although the position shifts in the Raman peaks of pyroxene, olivine, and quartz are very minor within the temperature range anticipated for the Raman measurements during the ExoMars mission, a detailed characterization of the temperature effects is needed in order to extract accurate information on the composition of solid solution minerals, e.g. pyroxene and olivine, and the information on structural stress and crystallinity for quartz.

Application II: LIBS Spectroscopic Study of Sulfur-Bearing Materials inside the Peach

LIBS uses atomic spectral lines to determine the elemental composition and elemental concentrations in most solids, liquids, and gases. As the LIBS technique involves the generation and expansion of a plasma plume near the surface of the sample, LIBS measurements are affected by the atmospheric pressure of the environment surrounding the sample. Taking into consideration a series of processes that include collisional excitation and target ablation, it has been demonstrated that the optimal atmospheric pressure for LIBS measurements is in the range 1–100 mbar.^[53] Along with atmospheric pressure, atmospheric composition plays another major role in LIBS elemental detection. Under Earth conditions, the strong LIBS excitation laser pulse ionizes the atmosphere surrounding the sample, producing electronically excited oxygen along with nitrogen. In the particular case of sulfur-bearing materials (which are of utmost importance for habitability studies on Mars), electronically excited S in the plasma can react with oxygen,^[54] reducing the strength of the S emission lines. Under the thin Martian atmosphere, a LIBS excitation laser pulse can break down the CO₂ and produce oxygen. However, much less oxygen is available on Mars for an eventual reaction with S from the plasma, making the S emission lines easier to detect. Another difficulty associated with the LIBS detection of sulfur is that the strongest S lines in LIBS emission are found in the vacuum UV (<200 nm) and the NIR (>900 nm) ranges.^[54,55] These regions are often beyond the detection capabilities of the detectors used in LIBS spectrometers, and only low-intensity S lines are observed in the visible region (400–600 nm). In our particular LIBS system, the spectral range is defined not only by the detector but also by the spectrograph design, which analyzes light in the 200–950 nm range only.

In order to assess the capability of our LIBS setup in the PEACH to detect sulfur in sulfur-bearing samples, we have collected LIBS spectra of pure sulfur and Fe₂(SO₄)₃·5H₂O at ambient pressure (1050 mbar air in our laboratory) and at Mars pressure (7 mbar CO₂). The spectra were collected with a 700 ns delay, and the integration time was set to 4 μs. The laser energy at the surface of the sample was measured as 30 mJ/pulse in a ~100 μm diameter spot. The spectrometer was wavelength-calibrated using ten atomic emission lines from a National Institute of Standards and Technology (NIST) traceable Hg/Ar lamp. In order to correct the overall spectral response of the whole system, especially the nonlinear efficiency of the dispersion grating in the spectrograph and spectral response of detector, an NIST-traceable dual deuterium/quartz tungsten halogen lamp was used as intensity standard. An average of five spots across the surface of the samples was analyzed; 25 single-shot spectra were recorded at each spot, yielding a total of about 125 spectra per sample.

The 550–570 nm regions of the LIBS spectra of crystalline sulfur exposed to each atmosphere are plotted in Fig. 12. Note that the spectrum acquired in 1050 mbar of air is dominated by

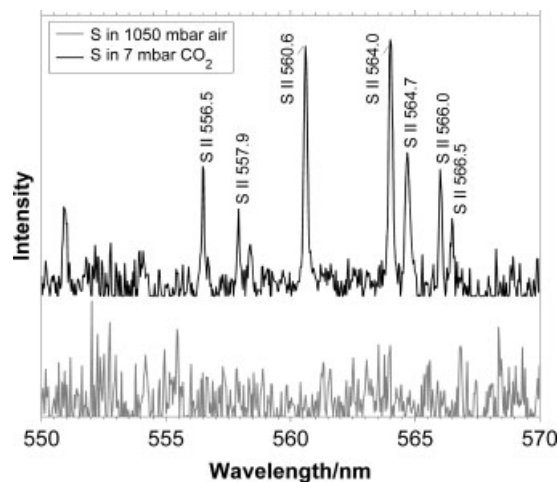


Figure 12. LIBS spectra of crystalline sulfur under laboratory (1050 mbar air) and Mars (7 mbar CO₂) atmospheres.

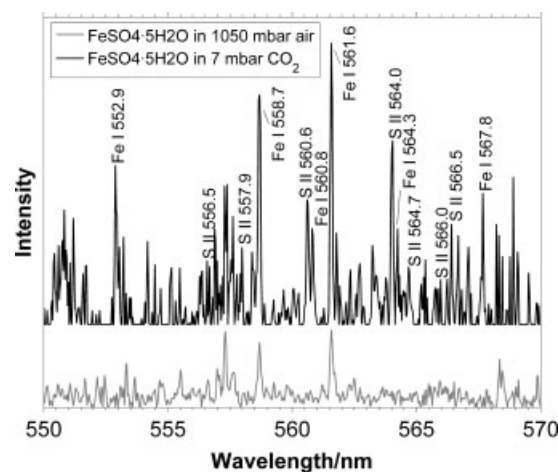


Figure 13. LIBS spectra of FeSO₄·5H₂O under laboratory (1050 mbar air) and Mars (7 mbar CO₂) atmospheres.

noise and does not feature detectable emission lines, whereas the lines at 556.5, 557.9, 560.6, 564.0, 564.7, 566.0, and 566.5 nm, associated with the transition II of S atoms, are clearly visible in the spectrum of sulfur recorded in the PEACH under 7 mbar CO₂ Mars atmosphere. Figure 13 shows the LIBS spectra of Fe₂(SO₄)₃·5H₂O at ambient Earth atmospheric conditions and at Mars conditions in the 550–570 nm region. The spectra are more complex than those of pure sulfur plotted in Fig. 12 due to the presence of strong iron emission lines, which in most cases overlap with weak sulfur lines. However, some of the S lines in this spectral region are readily detected when the sample is exposed to 7 mbar CO₂. Iron lines are also more intense in Mars atmosphere due to the favorable pressure and composition conditions in comparison with Earth's. The results of this set of tests confirm the strong influence of the atmospheric pressure and composition in LIBS measurements and the benefits of performing LIBS analysis in a Mars-simulated environment.

We are currently developing data-processing routines for the spectral analysis of LIBS data, which include baseline subtraction, noise reduction, peak deconvolution, and peak quantification. Upon calibration with certified reference materials relevant to

Mars exploration, our LIBS setup in the PEACH, in combination with these data-processing routines, will be able to derive the elemental concentrations of samples under Martian conditions and might help characterize the Martian outcrops and regolith expected to be interrogated by the ChemCam instrument onboard MSL. This set of experiments and data processing will be described in a separate paper.

Summary and Future Applications

The newly developed PEACH at Washington University in St. Louis allows us to conduct coordinated Raman/LIBS/MIR/NIR/MI measurements on the same set of minerals under simulated planetary environmental conditions; the temperature range inside the PEACH is 21 to -100°C and the pressure range is 1050–0.07 mbar, and virtually any gas mixture can be put in to simulate planetary atmospheric composition. The unique combination of contextual microimaging and multiple spectroscopic sensing allows *in situ* detailed characterization of samples under simulated planetary atmospheres. In particular, the Raman spectroscopic measurements inside the PEACH reported here have demonstrated the potential to monitor, and more importantly to quantify, the effect of temperature changes in the Raman spectra of minerals relevant to Mars.

We are designing a series of experiments to investigate other effects such as amorphization, dehydration/rehydration, and phase transitions of magnesium and iron sulfates as a function of temperature and atmospheric pressure and composition inside the PEACH which might help understand, for instance, the kinetics of these mechanisms on Mars. Among others, we are planning to investigate the stability of magnesium and iron sulfates at extremely low RH ($\sim 0\%$ RH), low temperature (-10°C) in Mars-like atmosphere, and the rate of amorphization of ferric sulfates at different temperatures to evaluate its occurrence on Mars. We also expect to obtain a set of Raman, LIBS, and IR spectra from a variety of Mars-relevant secondary minerals at low temperature and RH. These spectral databases will be useful for mission data interpretations, including Pancam-like instruments (MER, Phoenix), OMEGA (MEX), CRISM (MRO), as well as ChemCam (MSL), and Raman (ExoMars) in future missions.

Acknowledgements

This project was supported by a major financial support from the McDonnell Center for Space Sciences at Washington University in St. Louis, and partial supports from several NASA grants (#1295053 (MoO for ExoMars), NNX07AQ34G (MFRP), NNX10AM89G (MFRP), #39361-6452 (MER), NNG05GM95G (ASTID), #853076 (MRO), and #09-030 (MIDP)).

References

- [1] C. F. Chyba, C. B. Phillips, *Proc. Natl. Acad. Sci. USA* **2001**, 98, 801.
- [2] F. Raulin, *Space Sci. Rev.* **2008**, 135, 37.
- [3] J. P. Grotzinger, A. H. Knoll, *Annu. Rev. Earth Planet Sci.* **1999**, 27, 313.
- [4] J. F. Banfield, J. W. Moreau, C. S. Chan, S. A. Welch, B. Little, *Astrobiology* **2001**, 1, 447.
- [5] K. C. Benison, E. A. Jagniecki, T. B. Edwards, M. R. Mormile, M. C. Storie-Lombardi, *Astrobiology* **2008**, 8, 807.
- [6] J. Miot, K. Benzerara, M. Obst, A. Kappler, F. Hegler, S. Schadler, C. Bouchez, F. Guyot, G. Morin, *Appl. Environ. Microbiol.* **2009**, 75, 5586.
- [7] M. Craig, E. A. Cloutis, T. Mueller, Lunar and Planetary Institute Science Conference Abstracts, **2001**, 32, abstract # 1368.
- [8] D. W. G. Sears, P. H. Benoit, S. W. S. McKeever, D. Banerjee, T. Kral, W. Stites, L. Roe, P. Jansma, G. Mattioli, *Planet. Space Sci.* **2002**, 50, 821.
- [9] E. Mateo-Marti, O. Prieto-Ballesteros, J. M. Sobrado, J. Gomez-Elvira, J. A. Martin-Gago, *Meas. Sci. Technol.* **2006**, 17, 2274.
- [10] T. Encrenaz, T. K. Greathouse, B. Bezard, T. Fouchet, F. Lefevre, F. Montmessin, M. Bitner, A. Kruger, M. J. Richter, J. H. Lacy, F. Forget, S. K. Atreya, *A & A* **2010**, 520, A33.
- [11] C. S. Cockell, D. C. Catling, W. L. Davis, K. Snook, R. L. Kepner, P. Lee, C. P. McKay, *Icarus* **2000**, 146, 343.
- [12] A. S. Yen, B. Murray, G. R. Rossman, F. J. Grunthaler, *J. Geophys. Res. Planets* **1999**, 104, 27031.
- [13] E. A. Cloutis, M. A. Craig, J. F. Mustard, R. V. Kruzelecky, W. R. Jamroz, A. Scott, D. L. Bish, F. Poulet, J. P. Bibring, P. L. King, *Geophys. Res. Lett.* **2007**, 34.
- [14] A. Fedorova, O. Korablev, J. L. Bertaux, A. Rodin, A. Kiselev, S. Perrier, *J. Geophys. Res. Planets* **2006**, 111, E09S08.
- [15] F. Rull, *GeoRaman* **2010**, **2010**, abstract.
- [16] F. Rainer, E. A. Hildum, *NIST (National Institute of Standards and Technology) Special Publications* **1988**, 756, 74.
- [17] S. Saggese, W. Bratton, B. Fisk, Industry Partnerships to Deploy Environmental Technology, **1996**, abstract.
- [18] S. Maurice, R. C. Wiens, G. Manhes, D. A. Cremers, B. L. Barraclough, J. Bernardin, M. Bouye, A. Cros, B. Dubois, E. Durand, S. Hahn, D. Kouach, J.-L. Lacour, D. Landis, T. Moore, L. ParÄs, J. Platzler, M. Saccoccio, B. Salle, R. Whitaker, E. Stansbery, 36th Annual Lunar and Planetary Science Conference, **2005**, abstract.
- [19] J. J. Freeman, A. Wang, J. Lambert, Lunar and Planetary Institute Science Conference Abstracts, **2008**, 39, abstract # 2190.
- [20] A. Wang, J. J. Freeman, P. Sobron, J. Lambert, Lunar and Planetary Institute Science Conference Abstracts, **2010**, 41, abstract # 2018.
- [21] P. Sobron, J. J. Freeman, A. Wang, Lunar and Planetary Institute Science Conference Abstracts, **2009**, 40, abstract # 2372.
- [22] D. A. Long, *Raman Spectroscopy*, McGraw-Hill: New York, **1977**.
- [23] M. Balkanski, R. F. Wallis, E. Haro, *Phys. Rev. B* **1983**, 28, 1928.
- [24] C. Postmus, J. R. Ferraro, S. S. Mitra, *Phys. Rev.* **1968**, 174, 983.
- [25] G. E. Jellison, D. H. Lowndes, R. F. Wood, *Phys. Rev. B* **1983**, 28, 3272.
- [26] P. Sobron, F. Sobron, A. Sanz, F. Rull, *Applied Spectroscopy* **2008**, 62, 364.
- [27] D. W. Marquardt, *Curr. Contents/Eng. Technol. Appl. Sci.* **1979**, 14.
- [28] J. J. Niu, J. Sha, D. R. Yang, *Scr. Mater.* **2006**, 55, 183.
- [29] T. R. Hart, R. L. Aggarwal, B. Lax, *Phys. Rev. B* **1970**, 1, 638.
- [30] R. Tsu, J. G. Hernandez, *Appl. Phys. Lett.* **1982**, 41, 1016.
- [31] C. Ramaswamy, *Nature* **1930**, 125, 704.
- [32] S. A. Solin, A. K. Ramdas, *Phys. Rev. B* **1970**, 1, 1687.
- [33] X. Z. Zhao, K. A. Cherian, R. Roy, W. B. White, *J. Mater. Res.* **1998**, 13, 1974.
- [34] W. J. Borer, S. S. Mitra, K. V. Namjoshi, *Solid State Commun.* **1971**, 9, 1377.
- [35] A. Wang, J. J. Freeman, B. L. Jolliff, I. M. Chou, *Geochim. Cosmochim. Acta* **2006**, 70, 6118.
- [36] Z. C. Ling, A. L. Wang, *Icarus* **2010**, 209, 422.
- [37] E. Whalley, *Can. J. Chem. Rev. Can. Chim.* **1977**, 55, 3429.
- [38] C. H. Chio, S. K. Sharma, D. W. Muenow, *Spectrochim. Acta, Part A* **2005**, 61, 2428.
- [39] A. Wang, J. J. Freeman, I. M. Chou, B. L. Jolliff, *Geochim. Cosmochim. Acta* **2010**, submitted.
- [40] N. Krishnamurthy, V. Soots, *Can. J. Phys.* **1971**, 49, 885.
- [41] C. H. Chio, S. K. Sharma, D. W. Muenow, *Am. Mineral.* **2004**, 89, 390.
- [42] A. D. Rogers, P. R. Christensen, J. L. Bandfield, *J. Geophys. Res. Planets* **2005**, 110, E05010.
- [43] J. F. Mustard, F. Poulet, A. Gendrin, J. P. Bibring, Y. Langevin, B. Gondet, N. Mangold, G. Bellucci, F. Altieri, *Science* **2005**, 307, 1594.
- [44] H. Y. McSween, R. E. Arvidson, J. F. Bell, D. Blaney, N. A. Cabrol, P. R. Christensen, B. C. Clark, J. A. Crisp, L. S. Crumpler, D. J. Des Marais, J. D. Farmer, R. Gellert, A. Ghosh, S. Gorevan, T. Graff, J. Grant, L. A. Haskin, K. E. Herkenhoff, J. R. Johnson, B. L. Jolliff, G. Klingelhofer, A. T. Knudson, S. McLennan, K. A. Milam, J. E. Moersch, R. V. Morris, R. Rieder, S. W. Ruff, P. A. de Souza, S. W. Squyres, H. Wänke, A. Wang, M. B. Wyatt, A. Yen, J. Zipfel, *Science* **2004**, 305, 842.
- [45] A. Wang, B. L. Jolliff, L. A. Haskin, K. E. Kuebler, K. M. Viskupic, *Am. Mineral.* **2001**, 86, 790.

- [46] K. E. Kuebler, B. L. Jolliff, A. Wang, L. A. Haskin, *Geochim. Cosmochim. Acta* **2006**, *70*, 6201.
- [47] W. B. White, in *Infrared and Raman Spectroscopy of Lunar and Terrestrial Minerals*, (Ed.: C. Karr Jr), Academic Press: New York, **1975**, p 325.
- [48] N. Shimodaira, *Phys. Rev. B* **2006**, *73*, 214206.
- [49] A. Chopelas, *Am. Mineral.* **1991**, *76*, 1101.
- [50] B. Piriou, P. McMillan, *Am. Mineral.* **1983**, *68*, 426.
- [51] A. Wang, J. F. Bell, M. S. Rice, E. A. Cloutis, Lunar and Planetary Institute Science Conference Abstracts, **2008**, abstract # 2186.
- [52] K. J. Dean, W. F. Sherman, G. R. Wilkinson, *Spectrochim. Acta Part A* **1982**, *38*, 1105.
- [53] D. A. Cremers, in *Laser-Induced Breakdown Spectroscopy*, (Eds: J. P. Singh, S. N. Takhur), Elsevier: Amsterdam, **2007**, p 353.
- [54] L. Dudragne, P. Adam, J. Amouroux, *Appl. Spectrosc.* **1998**, *52*, 1321.
- [55] B. Salle, J. L. Lacour, E. Vors, P. Fichet, S. Maurice, D. A. Cremers, R. C. Wiens, *Spectrochim. Acta Part B* **2004**, *59*, 1413.
- [56] L. Haar, J. S. Gallagher, G. S. Kell, *National Standard Reference Data System (U.S.), NBS/NRC steam tables : thermodynamic and transport properties and computer programs for vapor and liquid states of water in SI units*, Hemisphere Publishing Corporation: Washington, DC, **1984**.